

Article

Structural Behavior of Massive Reinforced Concrete Structures Exposed to Thermomechanical Loads

Zhu Ma ¹, Changzheng Shi ^{1,*}, Hegao Wu ¹ and Songzi Liu ²

¹ State Key Laboratory of Water Resources and Hydropower Engineering Science, Wuhan University, Wuhan 430072, China; mazhu0518@whu.edu.cn (Z.M.); hgwu@whu.edu.cn (H.W.)

² Collage of Life Sciences, Wuhan University, Wuhan 430072, China; liusongzi@whu.edu.cn

* Correspondence: changzhengshi@whu.edu.cn

Abstract: Massive reinforced concrete (MRC) structures are utilized in a variety of applications where both mechanical and thermal properties are of concern. A 1:2 large-scale test model of the steel-lined reinforced concrete penstock (a kind of MRC) and a coupled thermomechanical numerical analysis are both implemented to investigate the thermomechanical effects on structural behavior. Three different temperature fields and eight temperature gradients are selected to explore how the temperature affects the crack width, steel stress, and deformation. The results show that the numerical simulation results are consistent with the experimental results and that this method can be applied to other similar MRC structure analysis. The thermal effect can cause 10^{-3} – 10^{-2} mm thermal crack width and ± 45 MPa thermal stress and this may lead the total crack width to exceed the limited value and the reinforcement stress beyond the yield strength. Consequently, the influence of the thermomechanical loads cannot be ignored and the corresponding temperature control measures must be taken to ensure structural safety and durability.

Keywords: thermal–mechanical coupling analysis; massive reinforced concrete structure; steel-lined reinforced concrete penstock; large-scale prototype model test; thermomechanical cohesive zone model; different temperature fields; crack width; finite element analysis



Citation: Ma, Z.; Shi, C.; Wu, H.; Liu, S. Structural Behavior of Massive Reinforced Concrete Structures Exposed to Thermomechanical Loads. *Energies* **2022**, *15*, 2671. <https://doi.org/10.3390/en15072671>

Academic Editor: F. Pacheco Torgal

Received: 10 March 2022

Accepted: 1 April 2022

Published: 6 April 2022

Publisher's Note: MDPI stays neutral with regard to jurisdictional claims in published maps and institutional affiliations.



Copyright: © 2022 by the authors. Licensee MDPI, Basel, Switzerland. This article is an open access article distributed under the terms and conditions of the Creative Commons Attribution (CC BY) license (<https://creativecommons.org/licenses/by/4.0/>).

1. Introduction

Massive reinforced concrete structures have been a commonly used type in civil engineering structures with the rapid development of China's national economy. The consequences of this type of structure collapsing would be unimaginable; thus, designing for their safety and durability is critical [1]. A steel-lined reinforced concrete penstock (SLRCP) is a typical kind of MRC structure mainly used in hydropower stations and diversion pipelines [2]. It is a composite structure of a steel liner and reinforced concrete, as shown in Figure 1. With the combined bearing of a steel liner and reinforced concrete, this composite penstock has an exceptional ability to bear high water pressure with less steel consumption [3]. Cracking is unavoidable under these structures' service conditions; however, crack widths should be controlled within the allowable value for their long-term use [4,5].

The penstock is exposed to a varying temperature field with the annual variation cycle under the action of water temperature inside the penstock and the air temperature outside the penstock during its long-term operation [6,7]. The differential expansion between the reinforcements and surrounding concrete causes thermal mismatch at the interface and may introduce extensive debonding in reinforced concrete [8,9]. As a result, under the simultaneous coupling effect of mechanical loading and heating/cooling, the thermal effects may be detrimental to MRC structures. However, there is limited research about the thermal–mechanical coupling analysis of MRC structures. Previous studies in other similar RC structures have proven that temperature changes have a significant effect on structural

behavior. Essam H et al. [10] conducted three temperature gradients—uniform, linear, and nonlinear—for finite element models to study the structural behavior of the reinforced concrete beams and frames. The results showed that the response of RC beams and frames was significantly based on the temperature gradients. Huang et al. [11] established a new software program named Safety Analysis During Construction Considering Temperature to analyze the effects of ambient temperature variations on RC structures and found that the temperature variations were significant and cannot be ignored. Moreover, the existing prototypes observation data of the SLRCPs have shown that the stress caused by temperature load is relatively large and will cause irreversible damage to the structure [12,13]. The crack width is also beyond the design value to reduce the service life of the penstock. The maximum crack widths of Dong-Jiang hydroelectric power plants (HPP), Wu-Qiang-Xi HPP, and Li-Jia-Xia HPP have reached 0.9 mm, 0.65 mm, and 1.40 mm respectively, which all exceed the limited design value of 0.3 mm [14]. This proves that it is far from enough to consider only the action of structural load in the safety and durability design of MRC structures. Therefore, a comprehensive investigation of temperature effects on MRC structural behavior is urgently need.

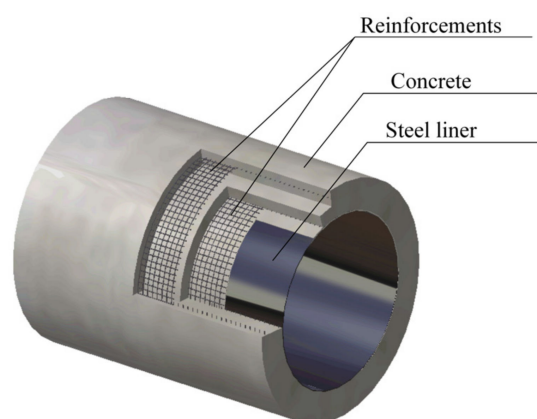


Figure 1. Schematic of the steel-lined reinforced concrete penstock.

There is no widely accepted empirical formula for the thermal cracking width or thermal stress of MRC structures due to their high geometric complexity and cracking nonlinearity [2]. Model test experiments are the most direct and effective method in MRC structure thermal–mechanical coupling analysis. A 1:2 large-scale prototype model test of the Three Gorges HPP has provided valuable and reliable data for the study of the temperature effects of MRC structures. However, the applications of the prototype test models are limited due to their high cost and time-consuming process. Therefore, the finite element approach is also utilized in this paper for the modeling and analysis of the MRC structures to investigate the influence of the coupling effect of thermal and mechanical loading on structural behavior compared with the experiment results. A cohesive crack model (CCM) [15–17] has been the commonly used crack model in concrete cracking analysis based on cohesive zone theory. This theory divides the crack into two parts: the true crack (fracture zone) and the virtual crack (fracture process zone). There is a relationship between the stress and opening displacement during the fracture process zone called the traction–separation law. Crack initiation and propagation are then determined by the traction–separation law and the true crack is then simulated by the separation of the top and bottom nodes of the cohesive elements. This model overcomes the disadvantages of traditional crack models. For example, the smeared crack model cannot obtain the crack width directly [18,19] and the element remeshing and node renumbering is required in the discrete crack model to follow the crack formation [20,21]. In recent years, several researchers [22–24] have improved the CCM to consider thermal effects in the concrete cracking analysis and these investigations have indicated that the coupled thermo-mechanical cohesive zone model is effective for thermal cracking simulation.

The objective of this paper is to study the structural response of the MRC structures subjected to thermal and mechanical loadings. A sequence of experimental tests is conducted in a 1:2 large-scale prototype model to investigate the effect of temperature gradients on the structural behavior of the SLRCP. In addition, a promising numerical method thermo-mechanical cohesive zone model is employed to simulate the thermal–mechanical process and the finite element results are verified by the experimental results.

2. Model Experiment Using a 1:2 Large-Scale Prototype

2.1. Description of Specimen

The Three Gorges HPP, as shown in Figure 2, with a total installed capacity of 18,200 MW is the largest in the world. It is in the Yangtze River in China and the diversion system is composed of 26 steel-lined reinforced concrete penstocks on the downstream side of the dam. The penstock is subjected to the internal water pressure, axis pressure, and temperature loads under service conditions. To ensure operation safety, it is necessary to explore the thermal–mechanical coupling effect on the structural behavior of the MRC structures. As a result, Wuhan University conducted a 1:2 large-scale prototype model to study the structural behavior of the SLRCP subjected to thermal and mechanical loadings.

Figure 3 shows the experimental section and specific dimensions of the test model. This model was designed according to geometric and physical similarity with a scale of 1:2. The plane dimension of this model is 12.5×12.5 m with a thickness of 0.6 m. The steel liner is selected as 16 Mn with a thickness of 16 mm. The reinforcement ratio of the test model is the same as the prototype model and three layers are arranged in the circular direction of the penstock with the spacing of 200 mm. A 15 mm PS cushion layer is arranged at the dam and penstock joint.

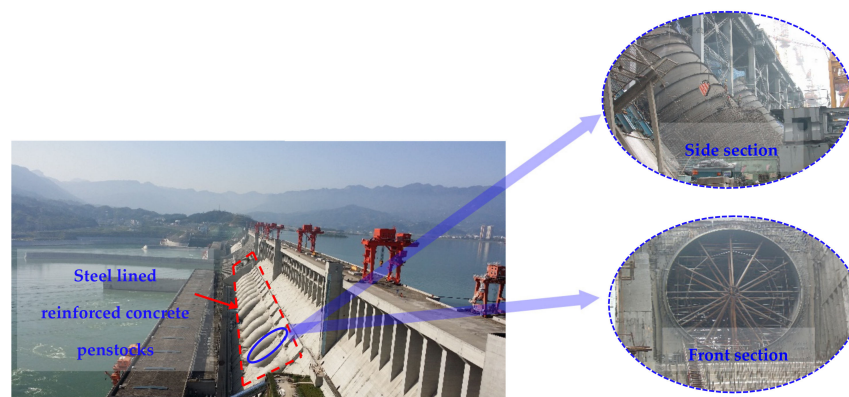


Figure 2. Steel-lined reinforced concrete penstock of the Three Gorges HPP.

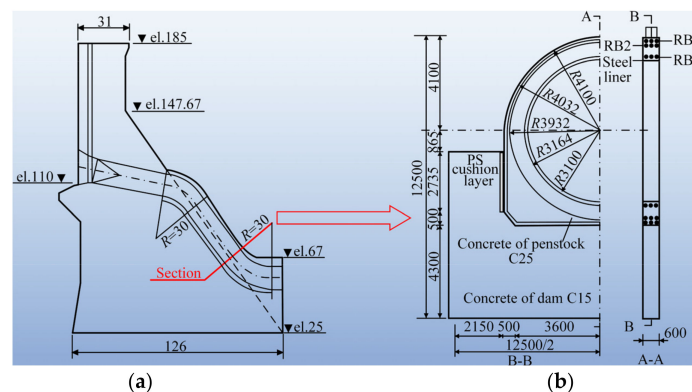


Figure 3. A 1:2 large-scale prototype model of the Three Gorges HPP: (a) penstock longitudinal profile (unit: m); (b) cross-section details of the penstock (unit: mm).

2.2. Material Properties of the Model

The test model was made of the same material as the prototype and the similarity coefficient of elastic modulus is 1. Particularly, the dam and penstock concrete aggregate was made of granite gravel utilized in the Three Gorges HPP. The concrete compressive strength was tested on six 200 mm cubes under standard conditions (temperature: 20 ± 2 °C relative humidity: $90 \pm 5\%$) for 28 d. The concrete tensile strength was established utilizing the splitting strength test on six 200 mm cubes. The limiting extended value of the concrete was tested on six concrete cuboids ($400 \times 100 \times 50$ mm). The material properties of the steel used in this model were determined by tensile testing at ambient temperature. The thermal properties of the concrete and steel were according to the standard GB 50010-2010. The material properties after converting to standard specimens are given in Table 1.

Table 1. Mechanical and thermal properties of the test model.

Material	Elastic (MPa)	Poisson Ratio	Compression Strength (MPa)	Tensile Strength (MPa)	Liner Coefficient Expansion	Specific Heat (kJ/kg·°C)	Heat Conductivity (W/(m·K))
Concrete of penstock	29,000	0.17	20.20	1.78	1.00×10^{-5}	0.96	1.28
Concrete of dam	24,000	0.17	14.60	1.00	1.00×10^{-5}	0.96	1.28
Steel liner	198,000	0.30	350 ¹	350 ¹	1.20×10^{-5}	0.46	60.00
Reinforcement	205,000	0.30	375 ¹	375 ¹	1.20×10^{-5}	0.46	60.00
PS cushion layer	0.4	0.30	/	/	8.00×10^{-5}	1.30	0.028

¹ The yield strength of the reinforcements.

2.3. Measuring Points Arrangement and Instruments

Eight sections (0° , 45° , 90° , 135° , 180° , 225° , 270° , and 315° , respectively) were designated to monitor the stress and deformation results of the steel liner and the reinforcements, as shown in Figure 4. Strain gauges were attached to the outside surface of the model 1/2 height; measuring points on the inner surface of the steel liner were located at 0° , 90° , 180° , and 270° ; and the strain gauges were also arranged at the above sections of the three layers of reinforcements. Four resistance thermometers, temperature measuring resistors, and crack measurement gauges were placed on the sections of 0° , 90° , 180° , 270° respectively to monitor the temperatures and thermal crack widths. The dial gauges were placed on the outer wall of the penstock at an interval of 45° to detect the penstock deformation.

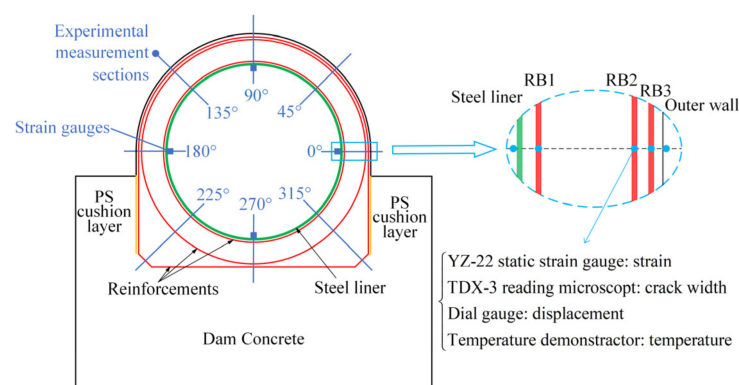


Figure 4. Longitudinal section schematic of the steel-lined reinforced concrete penstock.

2.4. Loading and Heating Test

Figure 5 demonstrates the loading device system. In particular, the mechanical load and temperature similarity coefficients are both 1. The electric oil pump was used to put pressure on the hydraulic steel pillow and then the pressure was evenly transmitted to the penstock. Before the formal experiment, the penstock was repeatedly loaded with 0.2 MPa pressure to check the device condition and zero pressure relief should be adjusted

after confirmation. The model was firstly loaded with 0.2 MPa, then the pressure was gradually to 0.6 MPa. To achieve a more precise crack initiation time, a 0.1 MPa increment in pressure was applied to the model until it reached a load of 1.21 MPa. To acquire a more accurate crack distribution and change in crack width, the model was tested with the design internal water pressure load of Three Gorges HPP of 1.21 MPa several times. The mechanical loading process of the model test is given in Figure 6.

The heating tests were conducted after the pressure loading test and both internal pressure load and thermal loads were applied to the test model. Massive reinforced concrete structures are mostly used in civil engineering structures and are exposed to natural conditions. The temperature schemes selected in this paper are based on the natural conditions of the Three Gorges HPP and the measured water and air temperature data [25–31] during the years of the Three Gorges are illustrated in Figure 7. It can be concluded that the seasonal temperature jumps and the variation rules during the years from 2004 to 2018 in The Three Gorges HPP are basically the same and the averages of them are close. The low air temperature period in the Three Gorges HPP is not long, mainly occurring from December to February. Furthermore, an average temperature below 5 °C rarely occurs. The air and water temperature in summer are lower than 30 °C. As a result, it is of little significance to study extreme temperature conditions for hydropower structures such as the SLRCP. There are three different temperature fields (the water temperature higher than the air temperature, the air temperature higher than the water temperature, and the water temperature is the same as the air temperature) of the steel-lined reinforced concrete penstock from the measured temperature data. Therefore, three similar temperature fields tests (Temperature field A: the inner wall temperature is lower than the outer, Temperature field B: the inner wall temperature is higher than the outer, and Temperature field C: the inner wall temperature is the same as the outer) were conducted.

It can be observed in Figure 7b,d that the maximum air and water temperature differences in 2007 of the steel-lined reinforced concrete penstocks were 22.5 °C and 17.65 °C respectively. The maximum temperature gradients are 8.96 °C and −5.38 °C separately from the measured data. As a result, eight temperature gradients were selected to further explore the temperature performance on the MRC structural behavior and the specific temperature gradients were given in Figure 8. The foam boards were laid on the surfaces of the model for insulation and the boundary temperatures of the model are 22.45 °C (A), 28.40 °C (B), and 28.00 °C (C) respectively. It can be shown that there were 30 electrothermal furnaces distributed in the air duct along the outer wall of the penstock. Moreover, to make the temperature variation uniform, two electric fans were installed at the outlet of the air duct. The hydraulic steel pillow was provided with tubes and filled with cooling water/heating oil to cool/heat the inner wall of the penstock. Consequently, temperature field A was easily formed by heating the outer wall of the penstock with the electrothermal furnaces and cooling the inner wall of the penstock with the cooling water. The temperature field B can also be realized by heating the inner wall with heating oil. Additionally, heating the inner and outer walls simultaneously can form the temperature field C.

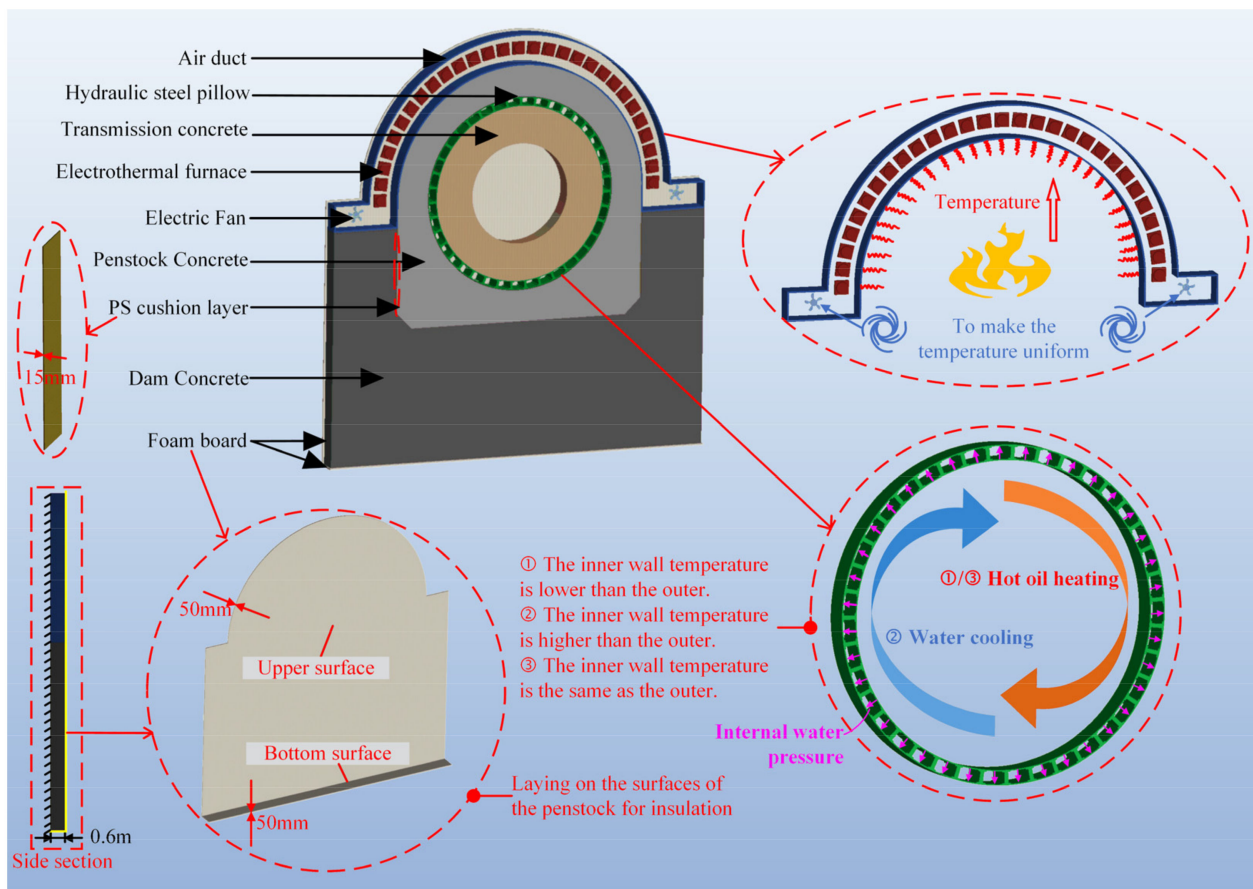


Figure 5. Loading device system.

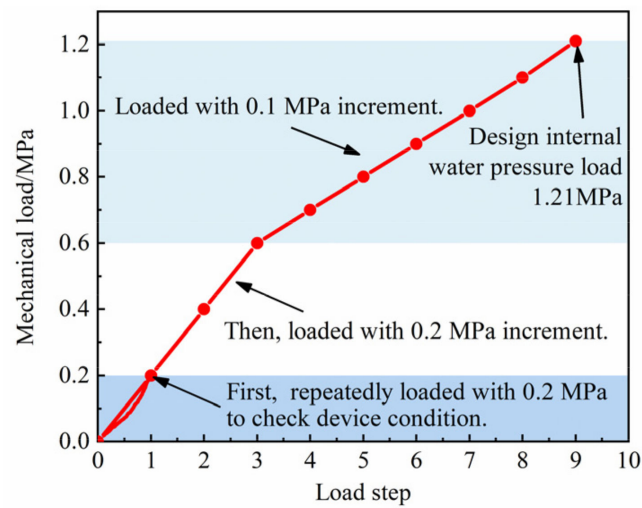


Figure 6. The loading process of mechanical load.

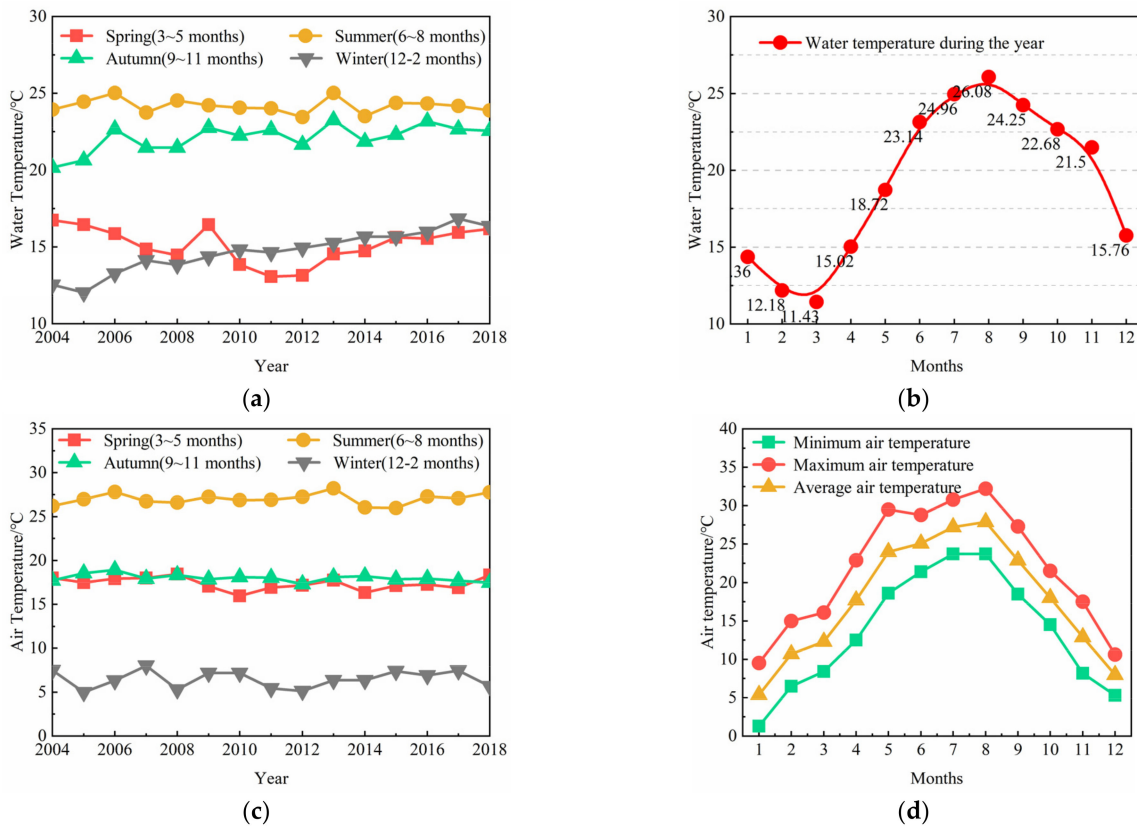


Figure 7. Measured temperatures data of the Three Gorges HPP: (a) the water temperatures from 2004 to 2018; (b) the water temperatures in 2007; (c) the air temperatures from 2004 to 2018; (d) the air temperatures in 2007.

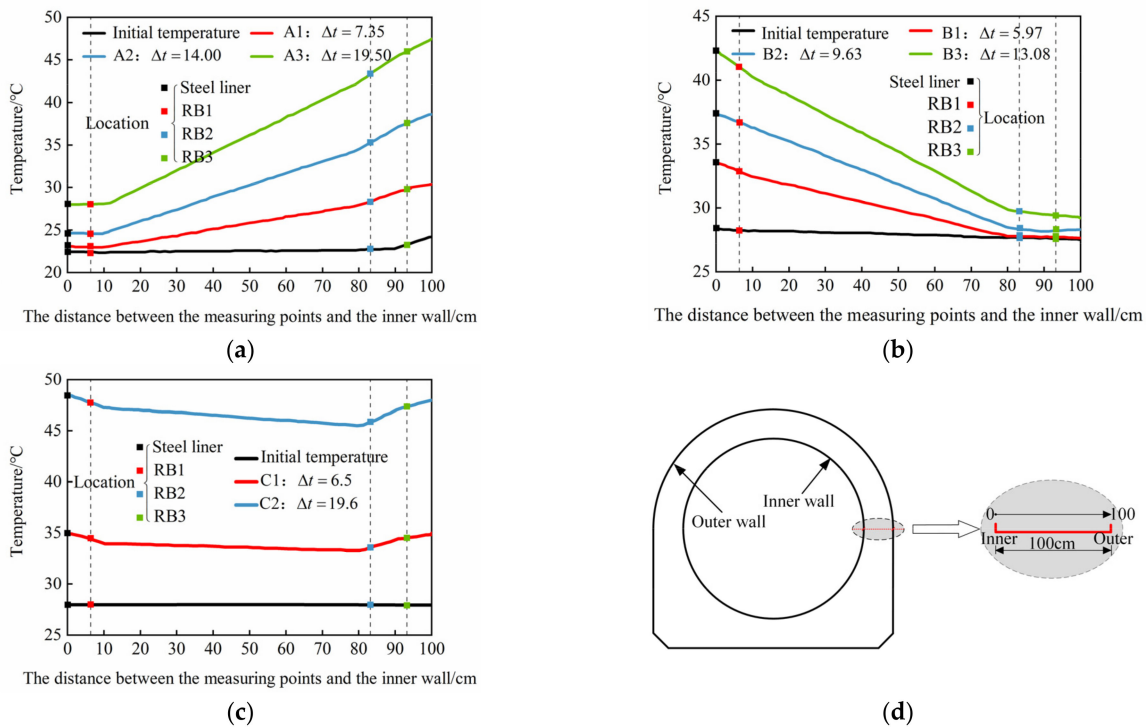


Figure 8. Temperature fields of the test model: (a) the inner wall temperature is lower than the outer; (b) the inner wall is higher than the outer; (c) the inner wall temperature is the same as the outer; (d) measuring points schematic.

2.5. Experimental Results

2.5.1. Crack Initiation and Propagation

The crack distribution and propagation (the subscript of the crack indexes indicates the crack initiation sequence and related mechanical load) results are illustrated in Figure 9. It can be found that the first crack was initiated at the left waist when the pressure reached 0.70 MPa and 20 radial cracks were finally distributed along with the circumferential distribution of the penstock. The cracking analysis is described in Section 3.3.1.

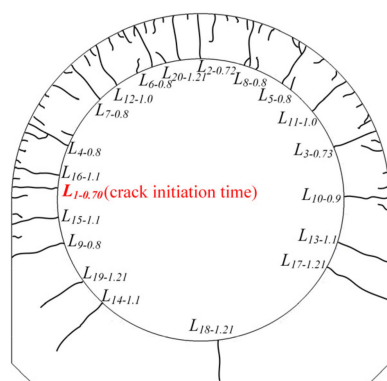


Figure 9. Crack distribution and propagation of the SLRCP.

2.5.2. Crack Width

The crack width under mechanical loads and thermal loads at the waists and crown are given in Table 2. It can be observed that the crack widths are largest in the middle which is consistent with the ‘eye’ shape of the crack. The specific discussion about the thermal crack width is in Section 3.3.1.

Table 2. Crack width (unit: 0.01 mm).

Crack Location		L ₁			L ₂			L ₃		
		Inner	Middle	Outer	Inner	Middle	Outer	Inner	Middle	Outer
P/MPa		7.80	30.00	20.40	10.00	42.30	13.20	8.84	48.80	15.70
Temperature field A	ΔT = 7.35 °C	2.20	0.50	−0.50	2.50	1.00	−0.50	8.00	1.00	−0.80
	ΔT = 14.00 °C	2.20	0.00	−1.00	3.20	0.80	−1.00	8.70	1.10	−1.00
	ΔT = 19.50 °C	3.50	1.00	−1.00	5.00	2.00	−1.00	9.50	1.00	−2.00
Temperature field B	ΔT = 5.97 °C	−1.00	3.00	1.00	0.00	1.00	1.00	0.00	2.00	1.00
	ΔT = 9.63 °C	−1.00	2.50	3.00	0.50	2.00	2.00	0.00	5.50	3.00
	ΔT = 13.08 °C	−1.00	3.50	4.00	1.00	3.00	2.50	0.00	8.00	4.50
Temperature field C	ΔT = 6.50 °C	0.00	1.00	1.00	1.20	2.00	0.00	0.00	4.00	1.00
	ΔT = 19.60 °C	0.00	5.00	5.00	4.80	5.00	2.00	0.00	8.60	3.00

2.5.3. Steel Stress

Tables 3–5 show the thermal steel stresses around the crack exposed to different temperature gradients. It can be concluded that the steel stresses near the cracks under the coupling effect of thermal and mechanical loading change with a range of ±45 MPa and may approach the yield strength. The analysis of the thermal stress is in the following Section 3.3.2.

Table 3. Thermal steel stress around the crack exposed to temperature field A (unit: MPa).

Crack Location	Gradients/°C	Steel Liner	RB1	RB2	RB3
L_1	7.35	9.00	2.50	−8.00	−12.00
	14.00	20.50	7.80	−20.50	−29.00
	19.50	23.00	9.30	−24.00	−35.00
L_2	7.35	5.50	4.50	−10.90	−11.20
	14.00	10.00	9.80	−21.50	−20.80
	19.50	13.60	14.50	−30.00	−27.20
L_3	7.35	12.00	7.20	−14.00	−8.00
	14.00	23.50	12.70	−26.70	−33.00
	19.50	26.50	16.00	−36.00	−44.00

Table 4. Thermal steel stress around the crack exposed to temperature field B (unit: MPa).

Crack Location	Gradients/°C	Steel Liner	RB1	RB2	RB3
L_1	5.97	−17.50	−8.00	13.80	11.80
	9.63	−23.00	−10.80	26.00	20.00
	13.08	−30.00	−17.00	40.00	34.00
L_2	5.97	−4.50	−2.00	4.90	5.00
	9.63	−8.00	−3.00	13.00	9.60
	13.08	−15.00	−4.50	17.50	9.80
L_3	5.97	−22.00	−6.00	17.00	9.50
	9.63	−29.00	−9.00	30.00	23.00
	13.08	−40.00	−12.00	45.00	38.00

Table 5. Thermal steel stress around the crack exposed to temperature field C (unit: MPa).

Crack Location	Gradients/°C	Steel liner	RB1	RB2	RB3
L_1	6.50	−7.00	2.50	6.00	5.00
	19.60	−21.00	3.50	27.00	25.50
L_2	6.50	1.40	4.80	2.00	4.00
	19.60	19.60	5.60	2.60	6.00
L_3	6.50	−19.00	2.00	12.00	3.50
	19.60	−21.80	3.50	19.50	8.00

3. Finite Element Modeling

3.1. Thermomechanical Cohesive Zone Model

The thermomechanical cohesive zone model is based on the cohesive zone theory which was first proposed by Dugdale [32] and Barenblatt [33]. This theory divides the crack into two parts [34,35] (Figure 10b): the virtual crack in the fracture process zone (FPZ) and the true crack in the stress-free zone. Furthermore, there is a certain relationship between stress and displacement in the FPZ called traction–separation law [36,37]. The key is to determine the traction separation law in the FPZ to determine the initiation and propagation of a crack. Consequently, this paper introduces a brief description of the traction separation law, combining both the thermal and mechanical effects in the flowing.

The thermomechanical cohesive zone model [38,39] provides additional coupling between thermal and stress analysis as material degradation taking place in the cohesive zone leading to changes both in load and heat transfer across the crack, as shown in Figure 10a. Cracks are considered as internal cohesive surfaces with mechanical loads and heat transfer capabilities in the thermomechanical cohesive zone model. Moreover, the mechanical equilibrium and energy balance must be fulfilled at the cohesive interfaces [23,40,41]. Based on the principle of virtual work, the mechanical equilibrium equation adding the contribution from the cohesive interface is written as

$$\int_{\Omega_0} \mathbf{S} : \delta \mathbf{F} dV - \int_{\Omega^-} \mathbf{T}_{cz} \cdot \delta \Delta dS = \int_{\Omega^+} \mathbf{T}_e \cdot \delta \mathbf{u} dS \quad (1)$$

where, $S = F^{-1} \det(F) \sigma$ means the nominal stress tensor; F is the deformation gradient; u is the displacement vector; T_{cz} is the traction stress vector; T_e is the traction vector on the external surface; $\Delta = u^+ - u^-$ is the displacement jump at the cohesive interface, “+” and “-” stands for the top and lower surfaces; Ω^+ and Ω^- represents the top and lower of the cohesive interface respectively.

In the same way, the thermal equilibrium following the principles of Fourier’s law is expressed by

$$\int_V \frac{\partial \delta \theta}{\partial x} k \frac{\partial \delta \theta}{\partial x} dV - \int_{S_{int}} q_{cz} \delta(\Delta \theta) dS = \int_{S_{ext}} \delta \theta q_e dS \tag{2}$$

where θ is the temperature; k is the conductivity matrix; q_e is the heat flux on the external surface; q_{cz} is the cohesive heat flux; $\Delta \theta = \theta^+ - \theta^-$ is the temperature jump at the cohesive interfaces.

Starting from the principles of thermodynamics stated above, a 3D finite element formulation is derived for a fully coupled simultaneous solution of the thermal field and the deformation field [42]. The eight-node cohesive element with three displacements degrees of freedom and additional degree freedom of temperature is demonstrated in Figure 8b,c [43]. The mechanical part realization of cohesive elements needs the derivative of the second term of Equation (1) and the cohesive forces are given as

$$\delta U_m = \int_{\Omega^+} [T_n \ T_t \ T_s] [\delta \Delta_n \ \delta \Delta_t \ \delta \Delta_s]^T dS \tag{3}$$

where, T_n , T_t , and T_s are the traction forces in three directions. Δ_n , Δ_t , and Δ_s are the displacement jump in three directions.

As for the thermal part, the implementation of the thermomechanical cohesive element requires the evolution of the first variation of the second term that can be expressed in Equation (2). The equation is given as

$$\delta U_{th} = \int_{S_{int}} dq_{cz} \delta(\Delta \theta) dS \tag{4}$$

where, the $q_{cz} = h_{cz} \Delta \theta$, and h_{cz} is the temperature conductance of the thermomechanical cohesive element.

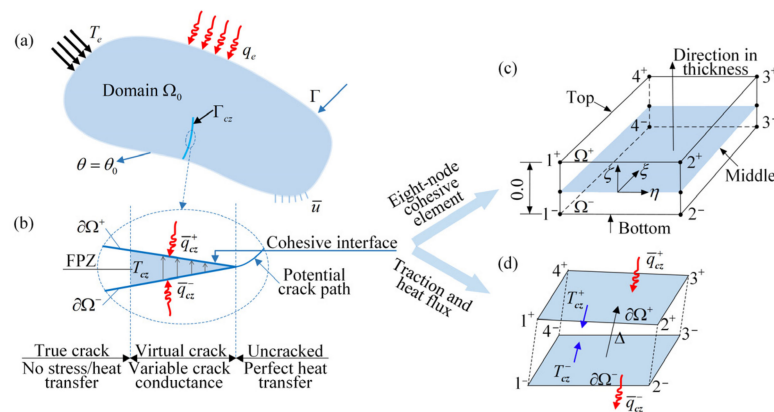


Figure 10. Schematic diagram of thermomechanical cohesive zone model: (a) solid body with the thermomechanical cohesive interface; (b) cohesive zone model; (c) eight–node cohesive element; (d) traction and heat flux in cohesive element.

The specific derivation of the nodal equation of the thermomechanical element can be found in [44–46]. There is just a brief introduction of the thermomechanical cohesive zone model in this paper, and the final element matrix considering both the mechanical and thermal properties is expressed as

$$S^E := \frac{\partial R^E}{\partial X^E} = \begin{bmatrix} -\frac{\partial T_{cz}}{\partial \Delta} & -\frac{\partial T_{cz}}{\partial \theta} \\ \frac{\partial h_{cz}}{\partial \Delta} & \frac{\partial h_{cz}}{\partial \theta} \end{bmatrix} \quad (5)$$

where, R^E and X^E are the residual and displacement vector of the cohesive element respectively.

3.2. Finite Element Model

The coupled thermomechanical numerical analysis of the composite penstock loaded with different temperature gradients and mechanical loads is described. A 3D finite element model based on the test model data is presented in Figure 11, both global and local systems are established to calculate the crack widths in the following analysis. Previous studies [3,12–14] have shown that the embedded model of reinforcements can obtain good simulation results and a perfect bond can be assumed between the reinforcements and concrete in the cracking analysis of the steel-lined reinforced concrete penstock. The cohesive elements are embedded throughout the mesh to simulate the random crack paths of the massive reinforced concrete structure. Additionally, the mesh must be fine enough in the thermomechanical cohesive zone model to ensure the crack initiation and propagation process [47]. Thus, after a mesh convergence study, the cohesive element size in this paper is settled as 0.1 m, which is 10^{-2} of the penstock dimensions. The coupled cohesive traction–separation law comprises not only stress degradation due to micro-cracking but also heat generation and energy transport [33,34] and the cohesive law used in this simulation is given in Figure 12. In this simulation, the material properties, temperature boundary conditions, and loading process of the penstock are the same as the test model, and the temperature fields obtained in ABAQUS under different temperature gradients can be seen in Figure 13.

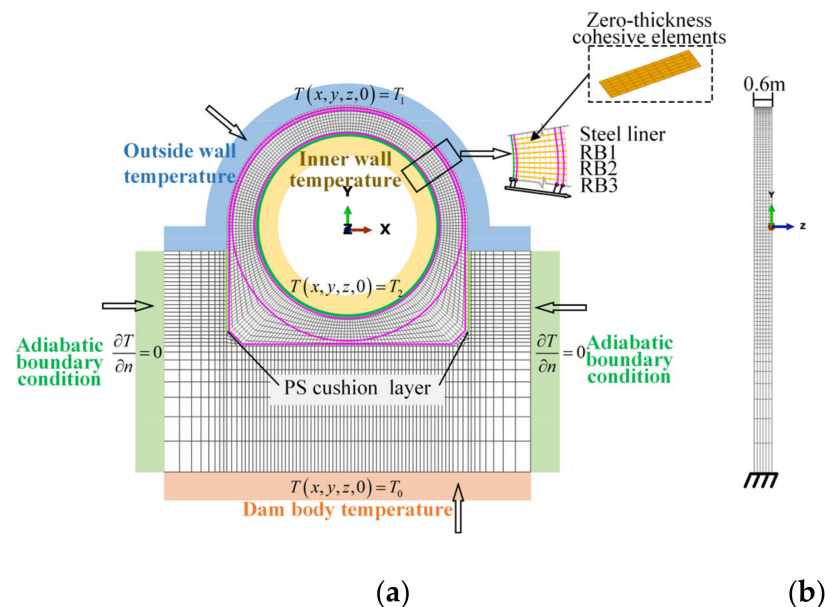


Figure 11. The 3D finite element model of the penstock: (a) front section and (b) side section.

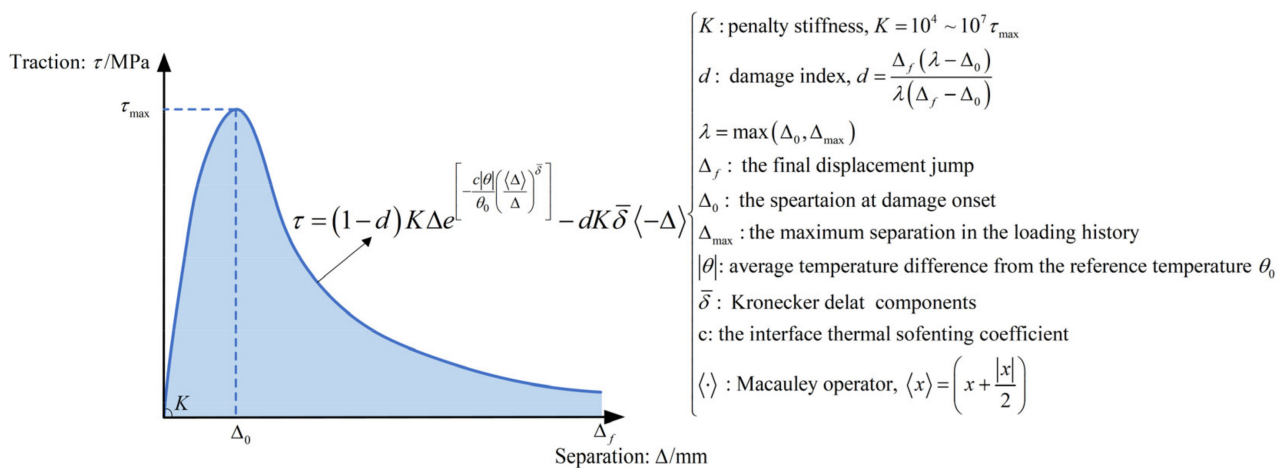


Figure 12. Coupled cohesive traction–separation law.

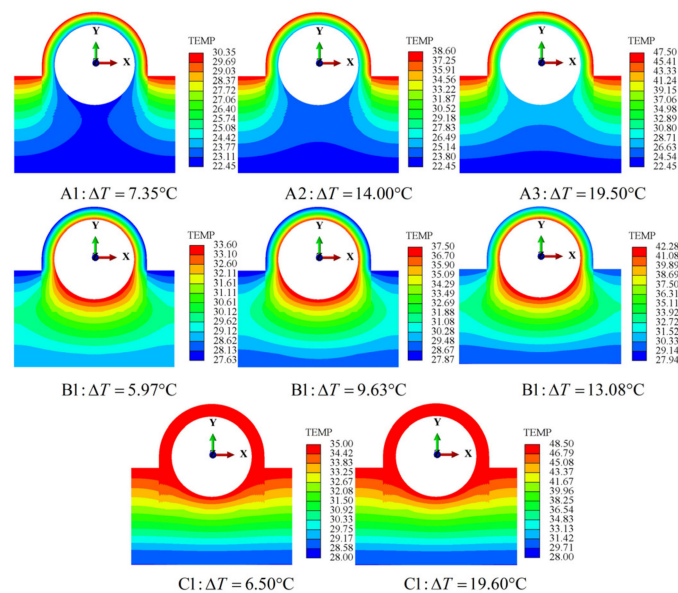


Figure 13. Temperature fields of the penstock exposed to different temperature gradients.

3.3. Structural Behavior

3.3.1. Thermal Crack Width

It is widely accepted that civil engineering structures are designed with high safety factors and it is hard for massive reinforced structures to reach a strength limit state. Large-scale civil engineering, practical experience, and experimental observations have proven that the composite penstock deteriorates faster in terms of serviceability than safety because of the reinforcement’s corrosion. Furthermore, reinforced concrete cracking is unavoidable. The crack widths should be limited to ensure the durability of the massive reinforced concrete structures [48]. Therefore, the following discussion will focus on the crack width exposed to the thermal–mechanical loads.

The numerical prediction results of the crack distribution and propagation are given in Figure 14a and the local amplification of the crack are also shown in Figure 14b. Compared with the experimental results in Figure 9, it can be observed that the cracks are both distributed along the circumference of the penstock with the crack initiation at the left waist and followed by the crown. The numerical maximum crack widths under mechanical loads match the experimental results well with the differences of 1.33% (L_1), 15.26% (L_2), and 8.23% (L_3).

As for the crack widths subjected to different temperature fields (Figure 15), the crack width variations are similar to the experimental results: the inner crack width increases and the outer crack width decreases under temperature field A and the crack variation is opposite in temperature field B. Furthermore, both the inner and outer crack widths increase under temperature field C. The crack width changes nonlinearly with the increase in temperature gradient and the crack width is the largest under temperature field C under the same temperature gradient. It can be concluded that the thermal crack width is between $\pm 10^{-3}$ and 10^{-2} mm as seen in Figure 15a–h. Although this variation is small, superimposition with the mechanical crack width will make some crack widths exceed their limit value and reduce their service life.

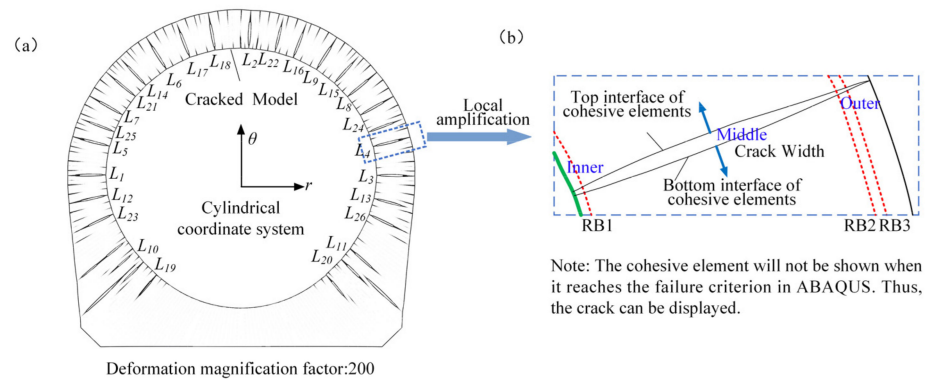


Figure 14. Crack propagation in thermomechanical cohesive zone model: (a) crack distribution; (b) calculation theory of the crack width.

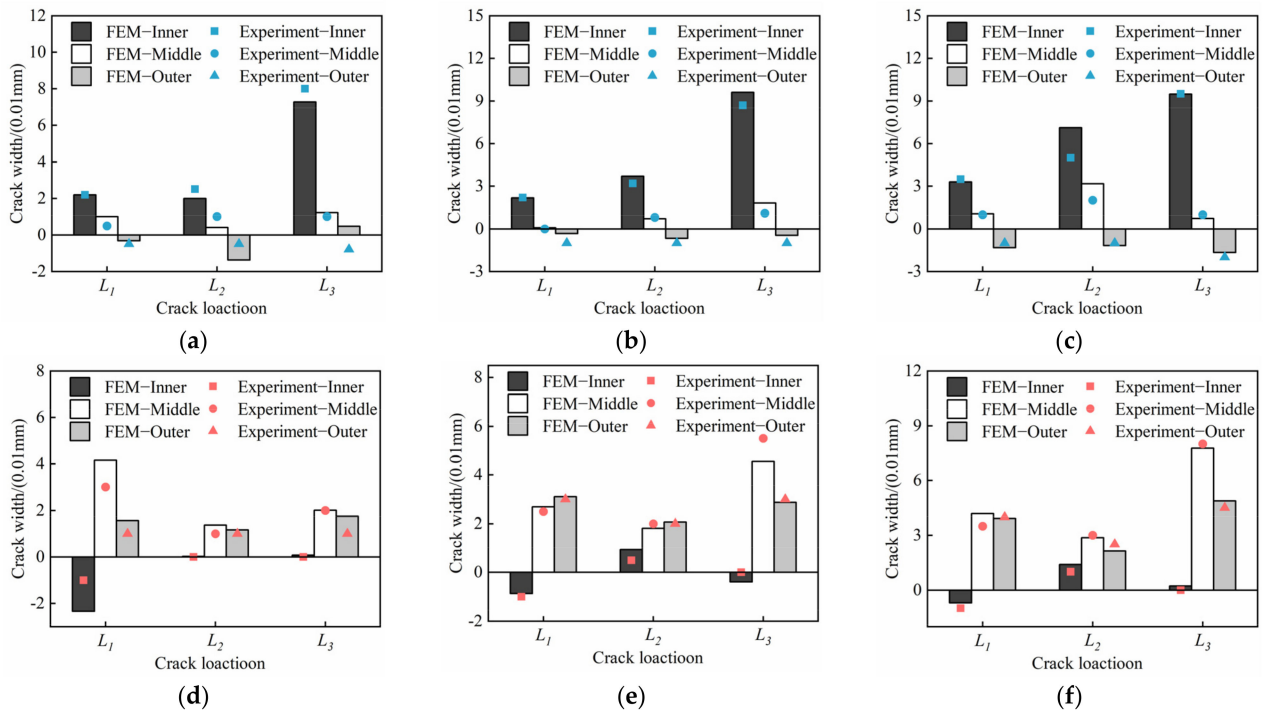


Figure 15. Cont.

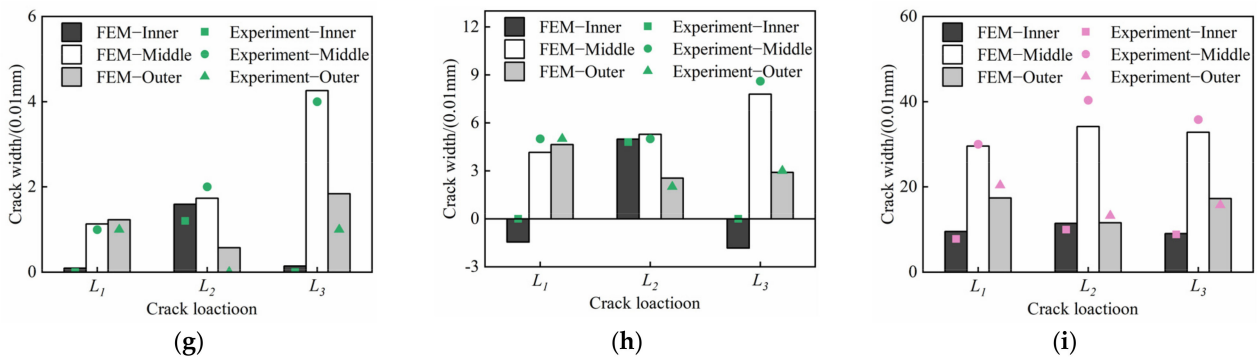


Figure 15. Crack widths under finite element model and test model subjected to different temperature gradients: (a)A1; (b) A2; (c) A3; (d) B1; (e)B2; (f) B3; (g) C1; (h) C2; (i) internal water pressure.

3.3.2. Thermal Stress of Steel

The temperature mainly affects the stress around the crack rather than the uncracked zones, thus the thermal stresses near several special cracks are recorded in Figure 16. The reinforcement RB1 is under tensile stress in temperature field A and the RB2/RB3 are under compressive stress which is consistent with the thermal crack width variations. The thermal stress variation phenomenon under temperature B is also opposite to the temperature field A. It can be found that the experimental data points are close to the numerical prediction curves and the thermal stress increases nonlinearly with the temperature gradient within ± 45 MPa. Take the stresses around crack L_1 in temperature field A2 as an example, the thermal stresses error of the steel liner, RB1, RB1, and RB3 between the thermomechanical cohesive zone model and the experiment are 6%, 2%, 2%, and 13% respectively. The maximum tensile stress occurs around the crack L_3 under temperature field B1 and reaches 45 MPa. It is recognized that the steel stress near the crack is large enough due to the mutation and then the steel stress (288 MPa) under the thermal–mechanical loads approaches the yield strength (375 MPa). As a result, the reinforcements tend to be more unsafe and may exceed the yield strength during long-term operations. Consequently, temperature control measures must be taken in the design to reduce the structural damage caused by temperature.

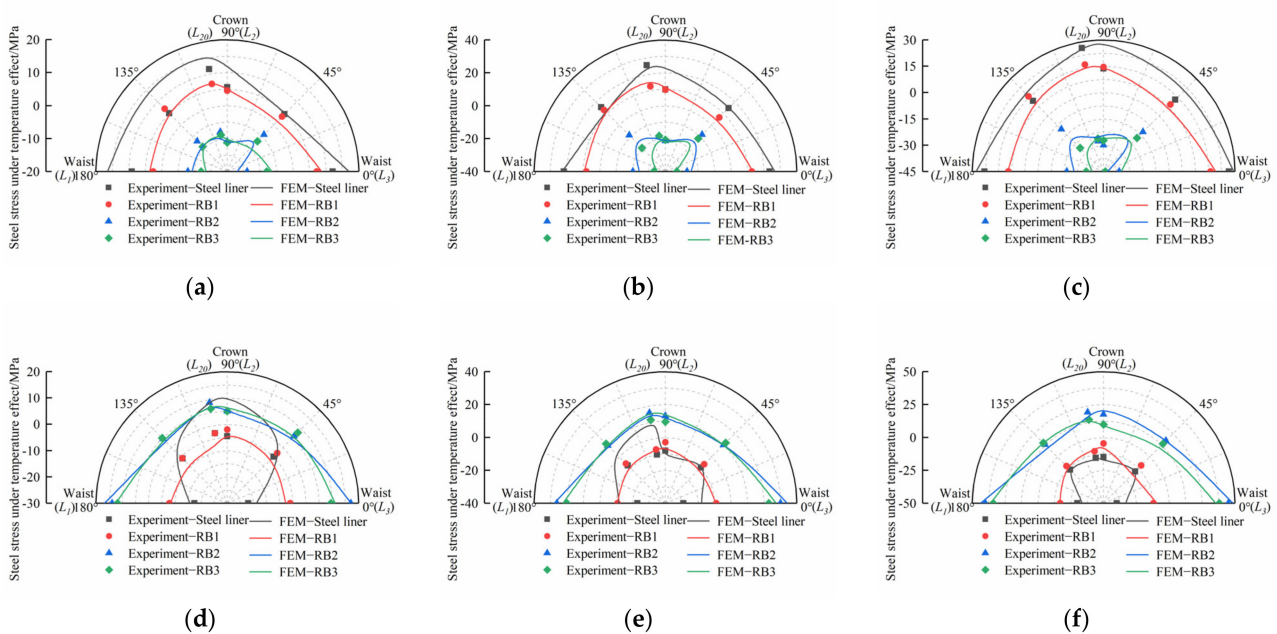


Figure 16. Cont.

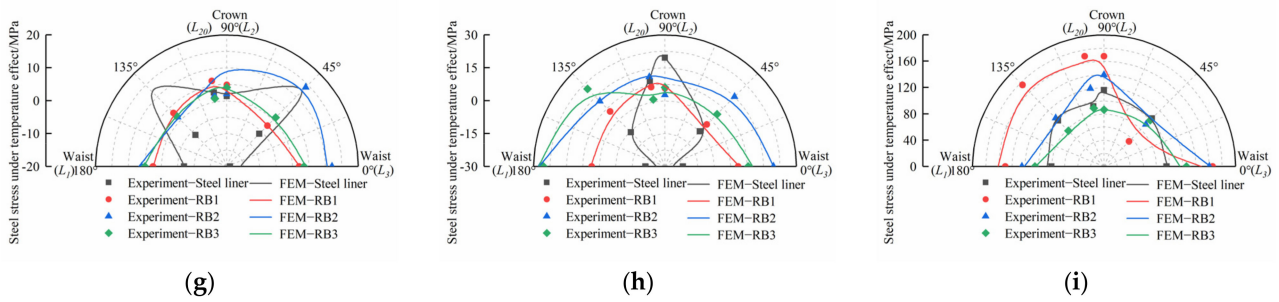


Figure 16. Thermal stress under finite element model and test model subjected to different temperature gradients: (a) A1; (b) A2; (c) A3; (d) B1; (e) B2; (f) B3; (g) C1; (h) C2; (i) internal water pressure.

3.3.3. Thermal Radial Displacement

The thermal radial displacements under exposure to different temperature fields are illustrated in Figure 17. Figure 17i shows that the penstock deforms radially outward under the coupling effect of internal water pressure and thermal loads. The penstock thermal expansion under temperature is well simulated by the thermomechanical cohesive zone model and the symmetric radial displacements are also modeled well due to the uniaxial symmetry of the geometry and load. In contrast to the thermal crack width and thermal stress, there exists a certain difference in the thermal radial displacement between the numerical predictions and the experimental results. However, the radial displacement results of the numerical model and the test model are still in the same order. From the perspective of the structural deformation, the thermal radial displacement under temperature C2 is 1.04 mm, which is basically equivalent to the mechanical displacement of 1.71 mm. The thermal deformation further results in a crack width increase, such as the crack increase in temperature field B3 is 0.045 mm, accounting for 22.5% of the total crack width, and the crack increase in temperature field C2 is 0.03 mm, accounting for 15% of the total crack width. The total crack width is then beyond the design value of 0.3 mm, which is detrimental to the safety of the penstock.

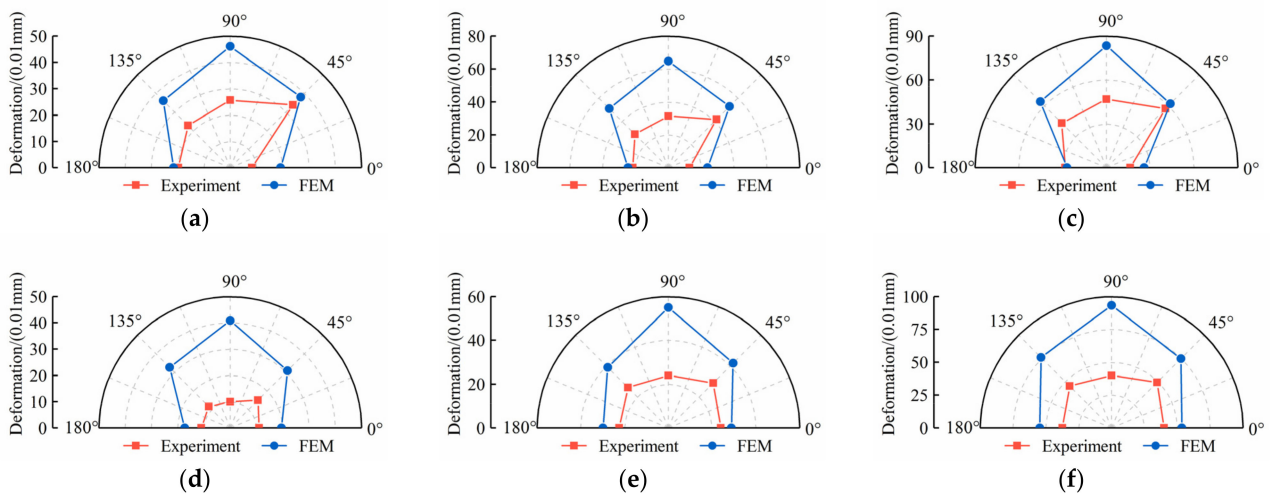


Figure 17. Cont.

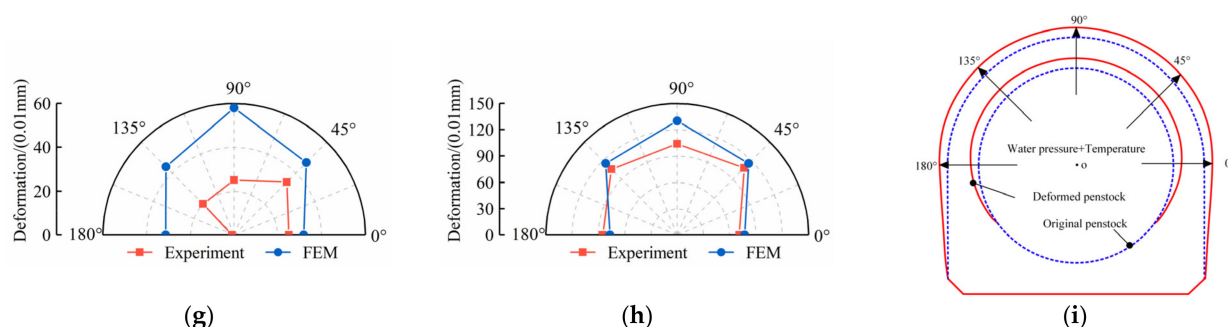


Figure 17. Radial displacement under finite element model and test model subjected to different temperature gradients: (a) A1; (b) A2; (c) A3; (d) B1; (e) B2; (f) B3; (g) C1; (h) C2; (i) internal water pressure.

4. Conclusions

A 1:2 large-scale prototype model of the Three Gorges HPP SLRCP is conducted to explore the structural response of MRC structures under thermo-mechanical loading. Three different temperature fields and eight temperature gradients are selected to further investigate the thermal phenomena of the MRC structures. In addition, based on the thermodynamics and cohesive zone theory, a novel finite element model thermomechanical cohesive zone model is formulated and utilized for thermo-mechanical analysis of the interface separation and heat transport of the composite penstock. Eight-node thermal cohesive zone elements are embedded throughout the mesh to realize and ensure a random cracking process of the penstock. The thermal and mechanical coupled cohesive law is proposed by extending the exponential cohesive law for the mode I modeling of the RC structure cracking. The thermomechanical coupling effect is implemented by the damage-dependent interface conductance and the thermal softening of the traction stress in the cohesive zone.

The crack initiation and propagation process, steel stress, and crack width obtained by the numerical method and experiment are in good agreement with each other. Based on the results and discussions presented in this paper, it can be concluded that temperature has an adverse effect on structural behavior. The thermal crack width around the cracks under different temperature gradients are between 10^{-3} and 10^{-2} mm and this leads the total crack width to exceed the limited value of 0.3 mm. The thermal stresses around the crack are within ± 45 MPa, and this results in the reinforcement stress approaching the yield strength. As a result, temperature control measurements must be taken to reduce the damaging effects of temperature and to consequently prolong the service life of massive reinforced concrete structures.

This paper provides valuable insight into the understanding of the coupling effect of thermal and mechanical loads on the steel-lined reinforced concrete penstocks and the effect of temperature on the structural response using a 1:2 large-scale prototype model test. These experimental results also verify the validation of the thermomechanical cohesive zone model in coupling thermomechanical analysis. It has been found that the numerical results are in good agreement with the experiment results, with an average difference of 6%. It can be concluded that this model can be employed to carry out coupled thermomechanical simulations of many other composites by changing the evolution cohesive law to describe particular materials and failure phenomena more accurately. As a result, more experiments on the thermomechanical analysis of reinforced concrete structures should also be designed and conducted to define the evolution of a cohesive law.

Author Contributions: Conceptualization, methodology, software, and formal analysis, Z.M., C.S. and H.W.; Original draft preparation, Z.M. and S.L.; Funding acquisition, C.S. and H.W. All authors have read and agreed to the published version of the manuscript.

Funding: This research was funded by the National Natural Science Foundation of China (no. 51409194).

Institutional Review Board Statement: Not applicable.

Informed Consent Statement: Not applicable.

Data Availability Statement: Not applicable.

Acknowledgments: The author would like to acknowledge the financial support of the National Natural Science Foundation of China Number (no. 51409194).

Conflicts of Interest: The author declares no conflict of interest.

References

- Guo, H.; Huang, L.; Song, W.; Wang, X.; Wang, H.; Zhao, X. Evaluation of the Summer Overheating Phenomenon in Reinforced Concrete and Cross Laminated Timber Residential Buildings in the Cold and Severe Cold Regions of China. *Energies* **2020**, *13*, 6035. [[CrossRef](#)]
- Ma, Z.; Shi, C.Z.; Wu, H.G. Numerical Cracking Analysis of Steel-Lined Reinforced Concrete Penstock Based on Cohesive Crack Model. *Structures* **2021**, *34*, 4694–4703. [[CrossRef](#)]
- Su, K.; Yang, Z.J.; Zhang, W.; Wu, H.L.; Zhang, Q.L.; Wu, H.G. Bearing Mechanism of Composite Structure with Reinforced Concrete and Steel Liner: An Application in Penstock. *Eng. Struct.* **2017**, *141*, 344–355. [[CrossRef](#)]
- Wu, H.; Ma, Z.; Shi, C. Overview of Research and Engineering Application of Steel-Lined Reinforced Concrete Penstocks Laid on Downstream Dam Surfaces. *Shuili Fadian Xuebao/J. Hydroelectr. Eng.* **2020**, *39*, 1–12. [[CrossRef](#)]
- El-Leathy, A.; Jeter, S.; Al-Ansary, H.; Abdel-Khalik, S.; Roop, J.; Golob, M.; Danish, S.; Alrished, A.; Djajadiwinata, E.; Al-Suhaibani, Z. Thermal Performance Evaluation of Two Thermal Energy Storage Tank Design Concepts for Use with a Solid Particle Receiver-Based Solar Power Tower. *Energies* **2014**, *7*, 8201–8216. [[CrossRef](#)]
- Gakhova, L.N. Temperature-Induced Stresses in Reinforced Concrete Structures. *IOP Conf. Ser. Earth Environ. Sci.* **2018**, *134*, 012021. [[CrossRef](#)]
- Zhe, D. Mathematical Model for the Opening and Closing of the Cracks on the Wall of Steel Lined Reinforced Concrete Penstocks Due to Thermal Load. *J. Hydraul. Eng.* **1996**, *11*, 1–5+13.
- Çavdar, A. A Study on the Effects of High Temperature on Mechanical Properties of Fiber Reinforced Cementitious Composites. *Compos. Part B Eng.* **2012**, *43*, 2452–2463. [[CrossRef](#)]
- Abdul-Rahman, M.; Al-Attar, A.A.; Hamada, H.M.; Tayeh, B. Microstructure and Structural Analysis of Polypropylene Fibre Reinforced Reactive Powder Concrete Beams Exposed to Elevated Temperature. *J. Build. Eng.* **2020**, *29*, 101167. [[CrossRef](#)]
- El-Tayeb, E.H.; El-Metwally, S.E.; Askar, H.S.; Yousef, A.M. Thermal Analysis of Reinforced Concrete Beams and Frames. *HBRC J.* **2017**, *13*, 8–24. [[CrossRef](#)]
- Huang, K.F.; Liu, X. La Effects of Temperature Variations on Safety of Reinforced Concrete Structures during Construction. *J. Shanghai Jiaotong Univ.* **2014**, *19*, 139–145. [[CrossRef](#)]
- Yang, P.; Shi, C.; Wu, H.; Liu, F.; Liu, T. Study on Temperature Effect and Thermal Insulation of Dam-Embedded Steel Penstock Encircled by Cushion Layer during Operation Period in Cold Region. *Sichuan Daxue Xuebao/J. Sichuan Univ.* **2016**, *48*, 47–54. [[CrossRef](#)]
- Shi, C.; Wu, H. Damage and Bearing Characteristics of Steel Lined Reinforced Concrete Penstock on Downstream Face of Dam in Hydropower Station. *Tianjin Daxue Xuebao/J. Tianjin Univ. Sci. Technol.* **2014**, *47*, 1081–1087. [[CrossRef](#)]
- Fu, J.Z. *Research on the Structure and Crack Width of the Steel-Lined Reinforced Concrete Penstock Laid on Downstream Dam Surfaces*; China Water & Power Press: Beijing, China, 2007.
- Segurado, J.; LLorca, J. A New Three-Dimensional Interface Finite Element to Simulate Fracture in Composites. *Int. J. Solids Struct.* **2004**, *41*, 2977–2993. [[CrossRef](#)]
- Elices, M.; Guinea, G.V.; Gómez, J.; Planas, J. The Cohesive Zone Model: Advantages, Limitations and Challenges. *Eng. Fract. Mech.* **2001**, *69*, 137–163. [[CrossRef](#)]
- Heidari-Rarani, M.; Ghasemi, A.R. Appropriate Shape of Cohesive Zone Model for Delamination Propagation in ENF Specimens with R-Curve Effects. *Theor. Appl. Fract. Mech.* **2017**, *90*, 174–181. [[CrossRef](#)]
- Edalat Behbahani, A.; Barros, J.A.O.; Ventura-Gouveia, A. Plastic-Damage Smeared Crack Model to Simulate the Behaviour of Structures Made by Cement Based Materials. *Int. J. Solids Struct.* **2015**, *73–74*, 20–40. [[CrossRef](#)]
- Dias-da-Costa, D.; Cervenka, V.; Graça-e-Costa, R. Model Uncertainty in Discrete and Smeared Crack Prediction in RC Beams under Flexural Loads. *Eng. Fract. Mech.* **2018**, *199*, 532–543. [[CrossRef](#)]
- Estay, D.A.; Chiang, L.E. Discrete Crack Model for Simulating Rock Comminution Processes with the Discrete Element Method. *Int. J. Rock Mech. Min. Sci.* **2013**, *60*, 125–133. [[CrossRef](#)]
- Lu, X.; Guo, X.M.; Tan, V.B.C.; Tay, T.E. From Diffuse Damage to Discrete Crack: A Coupled Failure Model for Multi-Stage Progressive Damage of Composites. *Comput. Methods Appl. Mech. Eng.* **2021**, *379*, 113760. [[CrossRef](#)]
- Hattiangadi, A.; Siegmund, T. A Thermomechanical Cohesive Zone Model for Bridged Delamination Cracks. *J. Mech. Phys. Solids* **2004**, *52*, 533–566. [[CrossRef](#)]
- Fleischhauer, R.; Qinami, A.; Hickmann, R.; Diestel, O.; Götze, T.; Cherif, C.; Heinrich, G.; Kaliske, M. A Thermomechanical Interface Description and Its Application to Yarn Pullout Tests. *Int. J. Solids Struct.* **2015**, *69–70*, 531–543. [[CrossRef](#)]

24. Jiao, Y.Y.; Zhang, X.L.; Zhang, H.Q.; Li, H.B.; Yang, S.Q.; Li, J.C. A Coupled Thermo-Mechanical Discontinuum Model for Simulating Rock Cracking Induced by Temperature Stresses. *Comput. Geotech.* **2015**, *67*, 142–149. [[CrossRef](#)]
25. Cao, G.; Hui, E.; Hu, X. Temperature in the Vicinity Area of Three Gorges Dam since the Three Gorges Reservoir Impounds. *J. Hydraul. Eng.* **2012**, *43*, 1254–1259. [[CrossRef](#)]
26. Du, L.-X.; Niu, L.-H.; Huang, T. Analysis of Water Temperature Variation and Its Influence in Three Gorges Reservoir. *Express Water Resour. Inf.* **2017**, *38*, 58–63. [[CrossRef](#)]
27. Xie, T.; Ji, D.; Liu, D.; Zhu, G.; Zhang, N. Water Temperature Monitoring of the Head of the Three Gorges Reservoir and Preliminary Analysis. *Resour. Environ. Yangtze Basin* **2013**, *22*, 1201–1206.
28. Ji, D.; Cheng, Z.; Long, L.; Yan, J.; Yang, Z. The Characteristics of Thermal Stratification in the Head Area of the Three Gorges Reservoir and Ecological Effects in Different Operation Periods. *Water Resour. Prot.* **2022**. Available online: <https://kns.cnki.net/kcms/detail/32.1356.TV.20220221.1412.005.html> (accessed on 1 March 2022).
29. Wang, Y.; Li, G.; Guo, Z.; Guo, Z. Spatial-Temporal Analysis of Monthly Air Temperature Changes from 1979–2014 in the Three Gorges Dam Region. *Yaogan Xuebao/J. Remote Sens.* **2018**, *22*, 487–496. [[CrossRef](#)]
30. Wang, R.; Tan, Y. Simulation and Projection of Temperature Change in Three Gorges Reservoir Based on High-Resolution Regional Climate Model. *Meteorol. Sci. Technol.* **2017**, *45*, 469–476+491.
31. Qin, Q.S. During Variation of Air Temperature in the Three Gorges Reservoir. *Meteorol. Sci. Technol.* **2002**, *30*, 304–305.
32. Dugdale, D.S. Yielding of Steel Sheets Containing Slits. *J. Mech. Phys. Solids* **1960**, *8*, 100–104. [[CrossRef](#)]
33. Barenblatt, G.I. The Mathematical Theory of Equilibrium Cracks in Brittle Fracture. *Adv. Appl. Mech.* **1962**, *7*, 55–129.
34. Paggi, M.; Wriggers, P. A Nonlocal Cohesive Zone Model for Finite Thickness Interfaces—Part II: FE Implementation and Application to Polycrystalline Materials. *Comput. Mater. Sci.* **2011**, *50*, 1634–1643. [[CrossRef](#)]
35. Hadjazi, K.; Sereir, Z.; Amziane, S. Cohesive Zone Model for the Prediction of Interfacial Shear Stresses in a Composite-Plate RC Beam with an Intermediate Flexural Crack. *Compos. Struct.* **2012**, *94*, 3574–3582. [[CrossRef](#)]
36. Alam, S.Y.; Kotronis, P.; Loukili, A. Crack Propagation and Size Effect in Concrete Using a Non-Local Damage Model. *Eng. Fract. Mech.* **2013**, *109*, 246–261. [[CrossRef](#)]
37. Wu, L.; Tjahjanto, D.; Becker, G.; Makradi, A.; Jérusalem, A.; Noels, L. A Micro-Meso-Model of Intra-Laminar Fracture in Fiber-Reinforced Composites Based on a Discontinuous Galerkin/Cohesive Zone Method. *Eng. Fract. Mech.* **2013**, *104*, 162–183. [[CrossRef](#)]
38. Willam, K.; Rhee, I.; Shing, B. Interface Damage Model for Thermomechanical Degradation of Heterogeneous Materials. *Comput. Methods Appl. Mech. Eng.* **2004**, *193*, 3327–3350. [[CrossRef](#)]
39. Peng, X.; Yong, H.; Zhang, X.; Zhou, Y. Analysis of Delamination and Heat Conductivity of Epoxy Impregnated Pancake Coils Using a Cohesive Zone Model. *Eng. Fract. Mech.* **2021**, *245*, 107555. [[CrossRef](#)]
40. Shu, W.; Stanciulescu, I. Fully Coupled Thermo-Mechanical Cohesive Zone Model with Thermal Softening: Application to Nanocomposites. *Int. J. Solids Struct.* **2020**, *188–189*, 1–11. [[CrossRef](#)]
41. Zreid, I.; Fleischhauer, R.; Kaliske, M. A Thermomechanically Coupled Viscoelastic Cohesive Zone Model at Large Deformation. *Int. J. Solids Struct.* **2013**, *50*, 4279–4291. [[CrossRef](#)]
42. Fagerström, M.; Larsson, R. A Thermo-Mechanical Cohesive Zone Formulation for Ductile Fracture. *J. Mech. Phys. Solids* **2008**, *56*, 3037–3058. [[CrossRef](#)]
43. Benabou, L.; Sun, Z.; Dahoo, P.R. A Thermo-Mechanical Cohesive Zone Model for Solder Joint Lifetime Prediction. *Int. J. Fatigue* **2013**, *49*, 18–30. [[CrossRef](#)]
44. Svolos, L.; Bronkhorst, C.A.; Waisman, H. Thermal-Conductivity Degradation across Cracks in Coupled Thermo-Mechanical Systems Modeled by the Phase-Field Fracture Method. *J. Mech. Phys. Solids* **2020**, *137*, 103861. [[CrossRef](#)]
45. Al-Amin, M.R.; Amin, M.R.; Sagor, R.H. Numerical Verification of the Dispersion Relation of Trapezoidally Corrugated Slow Wave Structure for Backward Wave Oscillators. *IET Microw. Antennas Propag.* **2018**, *12*, 313–319. [[CrossRef](#)]
46. Fleischhauer, R.; Behnke, R.; Kaliske, M. A Thermomechanical Interface Element Formulation for Finite Deformations. *Comput. Mech.* **2013**, *52*, 1039–1058. [[CrossRef](#)]
47. Van Mier, J.G.M.; Van Vliet, M.R.A. Influence of Microstructure of Concrete on Size/Scale Effects in Tensile Fracture. *Eng. Fract. Mech.* **2003**, *70*, 2281–2306. [[CrossRef](#)]
48. Li, Y.; Wang, J.-Z.K. Reliability Analysis of Crack Control Standard for Steel Lined Reinforced Concrete Penstock. *Yangtze River* **2018**, *49*, 103–107. [[CrossRef](#)]